MAGNETOTRANSPORT IMPACTON SHUNT RESISTANCEIN BIFACIAL c-Si CELLS: A NEAR-SHORT-CIRCUIT ANALYSIS

Manuscript Info

…………………….

Manuscript History
Received: xxxxxxxxxxxxxxxx
Final Accepted: xxxxxxxxxxxx
Published: xxxxxxxxxxxxxxxx

Key words: -
bifacial polycrystalline-silicon solar cell; shunt resistance; magnetic field; carrier-collection velocity; base thickness; illumination mode.

Abstract

……………………………………………………………

We analyze the influence of a weak magnetic field (B = 10^{-4} to 10^{-3} T) on the shunt resistance R_{sh} of bifacial polycrystalline-silicon solar cells, focusing on the near short-circuit region where the initial slope of the J-V curves sensitively reveals leakage. The device is modeled using a three-dimensional, grain-column approach. The transport equations are solved with diffusivity and diffusion length allowed to depend on B, while base thickness H (100-400 µm) and illumination mode (front, rear, dual) are swept systematically. Joint parameter extraction $\{J_0, n, R_s, R_{sh}\}$ is performed from the J-V characteristics and interpreted using standard experimental indicators (stability of the photocurrent plateau, low-voltage slope, evolution of the open-circuit voltage).

Three key findings emerge. (i) R_{sh} increases with the carrier-collection velocity and, in general, with B, but the magnitude of this change depends strongly on illumination geometry: rear illumination, where photogeneration is far from the junction, is the most sensitive; dual illumination instead yields higher and more stable R_{sh} thanks to bilateral injection that "seals" micro-leakage paths. (ii) Base thickness is a decisive lever: thinning toward ~100 µm tends to raise R_{sh} when surface passivation is effective, whereas a thicker base lengthens diffusion paths and amplifies the impact of surface/bulk defects and grain boundaries, especially under rear illumination. (iii) The field dependence is consistent with a magnetotransport mechanism: Lorentz-force deflection reduces effective mobility and diffusivity, modifies the low-voltage slope, and can increase the "apparent" R_{sh} extracted from J-V data.

Practically, the resulting maps R_{sh} (e,B) provide design targets (thickness and passivation) and metrology recommendations: prioritize high-quality passivation, exploit bifacial operation to limit leakage, and account for magnetic-field effects during measurements near V ≈ 0 to avoid misattributing magnetotransport-induced variations to diode parameters. Proposed extensions include assessing temperature effects, field orientation, and 3D reconstruction of leakage networks.This framework clarifies how magnetic environment, geometry, and illumination interact to set the effective leakage landscape in bifacial c-Si devices. By linking near-short-circuit diagnostics to physically grounded transport changes, it delivers actionable guidance for stabilizing R_{sh} and safeguarding performance under realistic operating conditions.

Introduction:-

Bifacial crystalline-silicon (c-Si) photovoltaics have become a mainstream route to higher energy yield, yet their performance still hinges on device geometry (notably base thickness), surface passivation, and parasitic resistances that shape the $J-V$ response under practical operating conditions [1]. While the impacts of series and shunt resistances on efficiency are well documented, through high-voltage slope changes and low-voltage leakage, respectively, the way these parameters evolve with illumination configuration (front, rear, dual) and base thickness remains a central design lever for bifacial cells [2]. In parallel, external magnetic fields can perturb carrier transport via Lorentz-force deflection, reducing mobility and diffusivity and thereby altering carrier collection; such magneto-transport effects have been observed in Si devices and modules, but their implications for the apparent shunt resistance extracted from $J-V$ curves are comparatively underexplored [3].

This work addresses that gap by focusing on the short-circuit neighborhood, where the photocurrent plateau ($\approx J_{sc}$) and the initial $J-V$ slope provide a sensitive window on leakage paths. Using a three-dimensional modeling and extraction framework, we quantify how the shunt resistance R_{sh} depends on base thickness and magnetic field, $R_{sh}(e,B)$, across the three illumination modes, and relate these trends to injection level, diffusion length, and surface recombination velocities (SRV) [4]. We further place R_{sh} variations in context with the co-evolution of the diode parameters$\{J_0,\ n\}$and with the series resistance R_s, leveraging voltage-dependent electroluminescence and lock-in thermography from the literature to interpret the local and distributed nature of leakage [5]. The resulting maps of $R_{sh}(e,B)$ and their physical interpretation provide actionable guidance for selecting thickness/passivation targets and for anticipating magnetic-field-induced performance drifts under front, rear, and bifacial operation.

Physical Model and Magnetic Parameters .1

i) Description of the Simulated Solar Cell

The analysis employs a three-dimensional columnar unit cell centered on a single polycrystalline-Si grain. A magnetic field, oriented normal to the junction plane, perturbs carrier transport. In this setting, the effective diffusion coefficient $D^*(B)$ and diffusion length $L^*(B)$ are, respectively:

$$D^*(B) = \frac{D}{1+(\mu B)^2} \tag{1}$$

$$L^*(B) = \sqrt{D^*.\tau} \tag{2}$$

Where :

1. D: diffusion coefficient in zero magnetic field (en $cm^2 \cdot s^{-1}$),
2. μ : charge-carrier mobility (en $cm^2 \cdot V^{-1} \cdot s^{-1}$),
3. B: magnetic flux density (tesla, T)
4. τ: minority-carrier lifetime (s)

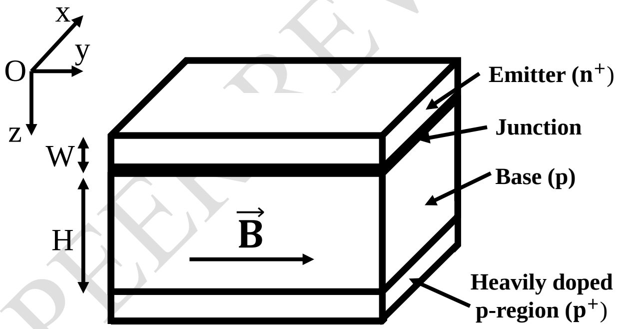

Figure 1. Simulated solar cell model.

As shown above, the bifacial cell is partitioned into four functional zones:

i) a thin n^+ emitter ($\approx\ 0.5 - 1\ \mu m$),
ii) the space-charge region (SCR) at the p–n junction,
iii) a p-type base, and
iv) a back-surface-field (BSF) layer.

For tractability, photogeneration in the emitter is taken negligible relative to that in the base, and any internal crystalline electric field within the base is disregarded; only the depletion-region field at the junction is retained. A three-dimensional coordinate system is used, with the junction placed at $z = 0$ and its plane defining the origin of (x, y). The base thickness H is treated as a control parameter in the range $100 - 400\ \mu m$. Under steady illumination, the minority-carrier continuity equation in the base reads:

$$\frac{\partial^2}{\partial x^2}\delta(x,y,z) + [1+(\mu B)^2]\frac{\partial^2}{\partial y^2}\delta(x,y,z) + \frac{\partial^2}{\partial z^2}\delta(x,y,z) - \frac{\delta(x,y,z)}{L^{*2}} = -\frac{G(z)}{D^*} \tag{3}$$

In this notation, D* is the diffusion coefficient and L* the diffusion length. The depth-dependent generation rate G(z) is given by (4):

$$G(z) \ = \ n\sum_{i=1}^{3} a_i e^{-b_i z} \tag{4}$$

a_i and b_i are coefficients obtained from modeling the photogeneration rate under the standard AM1.5 solar spectrum; n denotes the illumination level in suns.

The continuity equation then admits the general solution (5):

$$\delta(x,y,z) = \sum_j \sum_k Z_{j,k}(z) \cos C_j x \cos C_k(B) y \tag{5}$$

with :

$$C_k(B) = \frac{C_k}{C(B)} \tag{6}$$

By applying the boundary conditions at the grain boundaries, the coefficients C_k and C_j are determined as:

$$\left.\frac{\partial}{\partial x}\delta(x,y,z)\right]_{x=\pm\frac{g_x}{2}} = \mp\frac{S_g}{2D^*}\delta\left(\pm\frac{g_x}{2},y,z\right) \tag{7}$$

$$\left.\frac{\partial}{\partial y}\delta(x,y,z)\right]_{y=\pm\frac{g_y}{2}} = \mp\frac{S_g}{2D^*}\delta\left(x,\pm\frac{g_y}{2},z\right) \tag{8}$$

Define S_g as the recombination velocity at grain boundaries. Enforcing the boundary conditions on the transport equations yields two transcendental relations from which C_k and C_j are obtained, via graphical root finding or a numerical solver, namely:

$$\tan C_j \frac{g_x}{2} = \frac{1}{C_j} \times \frac{S_g}{2D^*} \tag{9}$$

$$\tan C_k(B) \frac{g_y}{2} = \frac{1}{C_k(B)} \times \frac{S_g}{2D^*} \tag{10}$$

Upon substitution of the general solution, the continuity equation becomes:

$$\frac{\partial^2}{\partial z^2} Z_{j,k}(z) - \frac{Z_{j,k}(z)}{{L_{j,k}^*}^2} = \frac{-G(z)}{D_{j,k}^*} \tag{11}$$

With :

$$\frac{1}{{L_{j,k}^*}^2} = C_j^2 + C_k^2 + \frac{1}{L^{*2}} \tag{12}$$

$$\frac{1}{D_{j,k}^*} = \frac{16\sin(C_j\frac{g_x}{2})\sin(C_k(B)\frac{g_y}{2})}{D^*\left[C_j g_x + \sin(C_j g_x)\right]\left[C_k(B) g_y + \sin(C_k(B) g_y)\right]} \tag{13}$$

With$L_{j,k}^*$ and $D_{j,k}^*$ representing, respectively, the effective diffusion length and coefficient, Eq. (11) can be solved to give:

$$Z_{j,k}(z) = A_{j,k}\sinh\frac{z}{L_{j,k}^*} + B_{j,k}\cosh\frac{z}{L_{j,k}^*} + \sum_{i=1}^{3} k_i e^{-b_i z} \tag{14}$$

With :

$$k_i = -\frac{n}{D_{j,k}^*}\frac{a_i {L_{j,k}^*}^2}{{b_i}^2 {L_{j,k}^*}^2 - 1} \tag{15}$$

The constants $A_{j,k}$ and $B_{j,k}$ are fixed by enforcing the junction and rear-surface boundary conditions as follows:

$$D^{*}\frac{\partial}{\partial z}\delta(x,y,z)=S_{f}\delta(x,y,z)\qquad \text{for } z=0 \tag{16}$$

$$D^{*}\frac{\partial}{\partial z}\delta(x,y,z)=-S_{b}\delta(x,y,z)\qquad \text{for } z=H \tag{17}$$

L andS_f be the effective front-surface recombination velocity, decomposed into an intrinsic junction part and a load-induced part:

$$S_f=S_{f0}+S_{fj} \tag{18}$$

S_{f0}denotes the intrinsic junction term associated with the leakage pathway (shunt resistance R_{sh}) at the junction [6,7], whereas S_{fj} represents the carrier flux imposed by the external load and therefore sets the operating point of the cell [6,7].

The parameter Sb corresponds to the effective recombination velocity at the rear surface of the solar cell.

Assessing the impact of an external magnetic field on the photovoltage in polycrystalline silicon is key to performance optimization: through the Lorentz force acting on electrons and holes, the field perturbs carrier trajectories and generally shortens the effective diffusion length, an effect that is especially pronounced for long carrier lifetimes [6]. The resulting change in photovoltage depends on device geometry and illumination scheme (front, rear, or bifacial).

In our numerical framework, we solve the standard semiconductor transport equations while allowing D and L to depend on the magnetic field B, consistent with device physics [1,8] and magnetotransport formulations reported in [7]. Surface-passivation effects are not modeled explicitly in this approximation and are assumed to play a negligible role in carrier collection [9].

Before presenting the main results, we specify the field-intensity window over which magnetic effects become appreciable: Figures 2 and 3 plot $D(B)$ and $L(B)$, respectively, thereby defining the operational range used in the subsequent simulations [7].

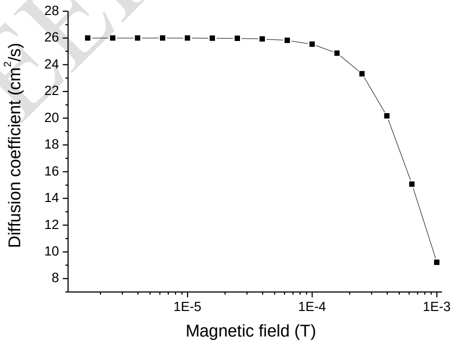

Figure 2. Variation of the carrier diffusion coefficient with magnetic field intensity.

For magnetic fields $B \lesssim 10^{-4}\,T$, the diffusion coefficient remains nearly constant at $\sim 25\,cm^2\,s^{-1}$. Beyond this threshold, D drops sharply to $\sim 10\ cm^2\,s^{-1}$, consistent with a pronounced reduction in mobility μ via the Einstein relation $D = (kT/q)\mu$.

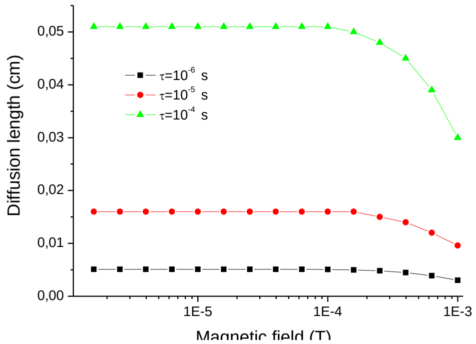

Figure 3. Evolution of the diffusion length as a function of magnetic field, for different carrier lifetimes.

Since $L = D\,\tau$, longer carrier lifetimes τ naturally produce larger diffusion lengths. For magnetic flux densities $B \lesssim 10^{-4}\,T$, however, L is essentially unchanged; a noticeable decrease appears only once B exceeds this $\sim 10^{-4}\,T$ threshold, with the strongest effect observed for long-lived carriers. These observations define the parameter window used here: we center on $B = 10^{-4}\,T$, where variations in mobility and diffusivity, and thus in photovoltage, are resolvable. Below $10^{-4}\,T$, magnetic perturbations stay within numerical scatter and lead to negligible shifts in V_{ph}; in the range 10^{-4} to $10^{-3}\,T$, the field is sufficient to reveal the coupling between magnetic perturbations and transport. Accordingly, the following simulations examine the combined influence of B and base thickness on the photovoltage, using this interval to quantify the device's magnetic susceptibility and to anticipate possible performance drifts under realistic industrial or environmental conditions.

Expression of the photogenerated current density J_{ph} $(A \cdot cm^{-2})$ .ii

For an illumination configuration $m \in \{Front, Rear, Dual\}$ a general form for J_{ph} is:

$$\mathrm{J_{ph,m}} = \frac{\mathrm{qD^*}}{\mathrm{g_x g_y}} \int_{-\frac{g_x}{2}}^{\frac{g_x}{2}} \int_{-\frac{g_y}{2}}^{\frac{g_y}{2}} \left[\frac{\partial}{\partial z}\delta_m(x,y,z)\right]_{z=0} dx.\,dy$$

Where :

- $\mathrm{J_{ph,m}}$: photogenerated current density for illumination mode mmm (in A·cm⁻²),
- q: elementary charge of the electron (1,602.10^{-19} C),
- D*: effective diffusion coefficient under the influence of the magnetic field (cm²/s),
- g_x, g_y: lateral dimensions of the simulation domain along the x and y directions (in cm),
- $\delta_m(x,y,z)$: excess minority carrier density induced by optical generation for mode m,
- $\left[\frac{\partial}{\partial z}\delta_m\right]_{z=0}$: derivative of the excess carrier density evaluated at the junction plane (z = 0).

Expression of the photovoltage (in V) .iii

For any illumination mode $m \in \{Front, Rear, Dual\}$, the photovoltage can be written as:

$$\mathrm{Vph}_{m} = V_T \ln\left(1 + \frac{1}{n_0} \int_{-\frac{g_x}{2}}^{\frac{g_x}{2}} \int_{-\frac{g_y}{2}}^{\frac{g_y}{2}} \delta_m(x, y, 0)\, dx\, dy\right) \quad (19)$$

With

$$V_T = \frac{KT}{q} \quad (20)$$

And

$$n_0 = \frac{{n_i}^2}{N_b} \quad (21)$$

where :

1). $V_{ph,m}$: Photovoltage for illumination mode m (in V),

2). V_T: Thermal voltage

3). K: Boltzmann constant

4). T: Absolute temperature (K)

5). q: elementary charge of the electron ($1{,}602.10^{-19}$ C),

6). n_0: Reference equilibrium minority carrier concentration (cm^{-3})

7). ${n_i}^2$: Intrinsic carrier concentration squared (cm^{-6})

8). N_b: Base doping concentration (cm^{-3})

9). D^*: effective diffusion coefficient under the influence of the magnetic field (cm²/s),

10). g_x, g_y: lateral dimensions of the simulation domain along the x and y directions (in cm),

11). $\delta_m(x, y, z)$: excess minority carrier density induced by optical generation for mode m,

12). $\left[\frac{\partial}{\partial z}\delta_m\right]_{z=0}$: derivative of the excess carrier density evaluated at the junction plane ($z = 0$).

Expression of the series resistance (in $\Omega \cdot \mathrm{cm}^{-2}$) .iv

Figure 4 shows the photocurrent density as a function of photovoltage under front-side illumination, with the other parameters held constant. The circled area highlights the nearly horizontal part of the curve, essentially insensitive to photovoltage, near short-circuit ($V \approx 0V$). This plateau appears in the same way on all curves obtained with other parameter sets, regardless of the illumination mode. In this regime, the cell behaves like a current source: the delivered current remains almost constant and corresponds to the short-circuit photocurrent density J_{sc}. Since a solar cell is not ideal, a residual leakage current is present; typicallysmall for good-quality devices, it is modeled by a shunt resistance R_{sh} representing an internal leakage path. The corresponding equivalent electrical circuit for operation in this regime is shown in Figure 5.

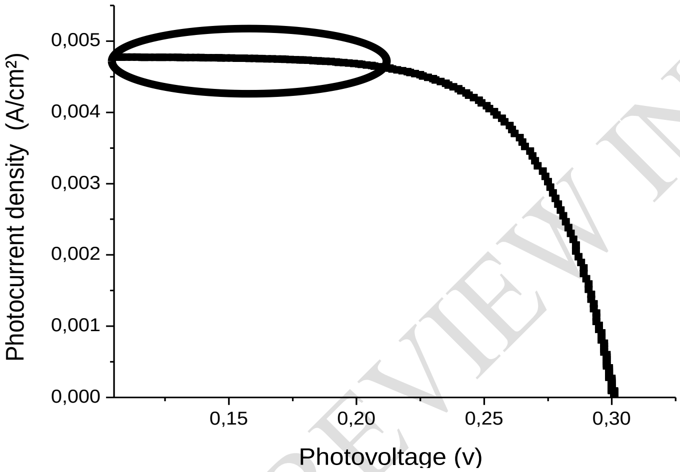

Figure 4: caractéristique J-V d'une cellule solaire ai silicium

Figure 5 presents the equivalent electrical circuit of a silicon solar cell operating in the short-circuit regime.

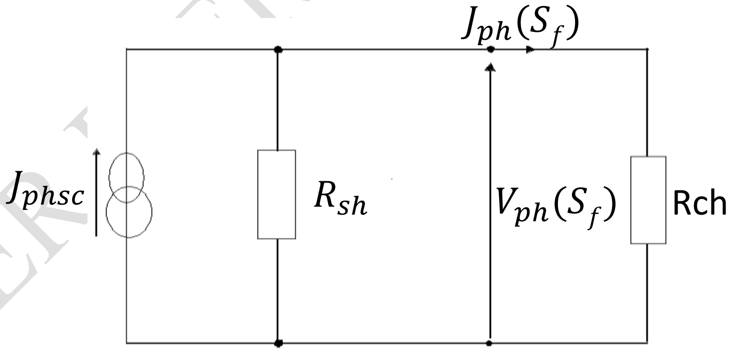

Figure 5: equivalent electrical circuit of the solar cell under short-circuit conditions

J_{phsc} .: short-circuit current density
R_{sh} : series resistance
J_{ph} : photocurrent
V_{ph} : photovoltage
R_{ch} : very small load resistance

Figure 5 shows an equivalent electrical circuit of a photovoltaic cell under short-circuit conditions. Applying Kirchhoff’s current law to this circuit gives:

$$\mathbf{V(S_f) = R_{sh}(I_{sc} - I_{ph}(S_f))} \qquad \mathbf{(22)}$$

From this expression, the shunt resistance follows and can be written as:

$$\mathbf{R_{sh}} = \frac{\mathbf{V(S_f)}}{\mathbf{I_{sc} - I_{ph}(S_f)}} \qquad (23)$$

RESULTS AND DISCUSSION .2

This study examines bifacial polycrystalline-silicon solar cells subjected to a modest magnetic flux density $B = 10^{-4}\ to\ 10^{-3}\ T$. Our analysis concentrates on operation near short circuit, where we quantify the short-circuit photocurrent density $\mathrm{J_{sc}}$ and the shunt resistance $\mathrm{R_{sh}}$ as functions of the carrier-collector velocity (CCV), the base thickness $H\ (100 - 400\ \mu m)$, and the illumination configuration (front, rear, or bifacial). Figures 6 and 7 plot the $\mathrm{J} - \mathrm{V}$ characteristics in the vicinity of $V \approx 0$ for $H = 100\ \mu m$ and $H = 300\ \mu m$, respectively, under different B. In this low-voltage window, the plateau value as $V \to 0$ provides $\mathrm{J_{sc}}$, while the initial slope of the curve yields an area-normalized estimate of the shunt resistance via:

$$\mathrm{R}_{\mathrm{sh},eff} \approx \left|\frac{dV}{dJ}\right|_{V\to 0}.$$

This representation isolates leakage-path effects (through $\mathrm{R_{sh}}$) from photogeneration-limited current flow, enabling a clean comparison of how CCV, base thickness, illumination mode, and the applied field B influence near-short-circuit behavior.

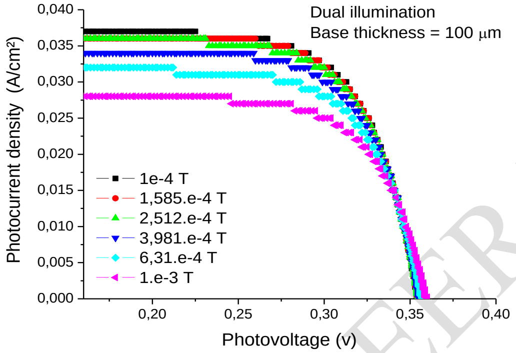

Figure 6: Photocurrent density as a function of photovoltage for different magnetic-field values

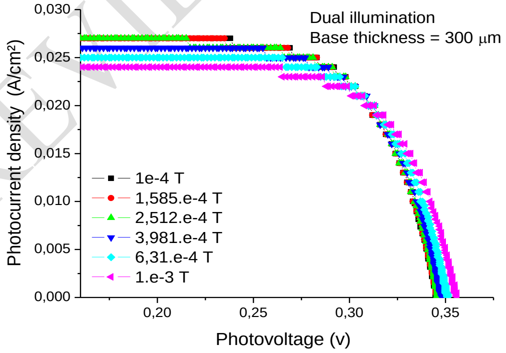

Figure 7: Photocurrent density as a function of photovoltage for different magnetic-field values

Under dual illumination, the $\mathrm{J_{ph}} - \mathrm{V_{ph}}$ curves for $H = 100\ \mu m$ (Fig. 6) and $H = 300\ \mu m$ (Fig. 7), as the magnetic field B increases from 10^{-4} to 10^{-3} T, show:

i) a drop in short-circuit photocurrent density that is more pronounced for the thinner base (~27%) than for the thicker base (~11%), with the highest initial value observed for $H = 100\ \mu m$ ($\mathrm{J_{sc}} \approx 0.037\ A \cdot cm^{-2}$); and

ii) a slight increase in the open-circuit photovoltage beyond 0.35 V, while at low $\mathrm{V_{ph}}$ the plateau $\mathrm{J_{ph}} \approx \mathrm{J_{sc}}$ persists before the rapid fall to zero at $\mathrm{V_{oc}}$. This behavior is attributed to Lorentz-force deflection of carriers, which reduces the effective diffusivity D and the diffusion length $L = \sqrt{D \cdot \tau}$, together with transport modifications akin to magnetoresistance that degrade carrier collection; these trends qualitatively agree with experimental observations and magneto-transport modeling on Si cells/modules [10, 11, 12]. The stronger attenuation for $H = 100\ \mu m$ is consistent with a magnetic-field-dependent optimum base thickness [13] and, more broadly, with reports on the influence of base thickness/diffusion path on J_{sc} [4]. Finally, the orientation of B relative to the carrier flux can modulate the magnitude of the degradation [14].

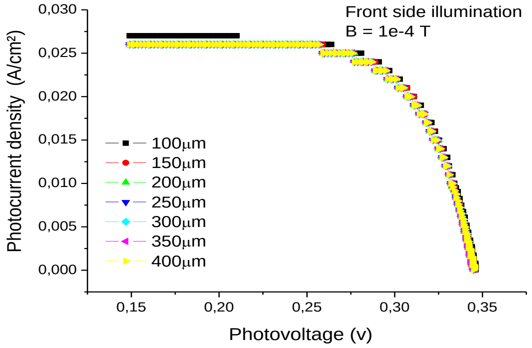

Figure 8: Photocurrent density as a function of photovoltage for various base thicknesses under front-side illumination

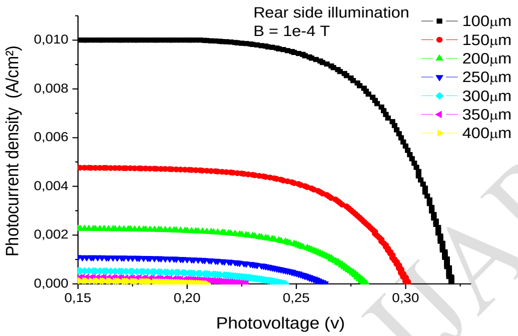

Figure 9: Photocurrent density as a function of photovoltage for various base thicknesses under rear-side illumination

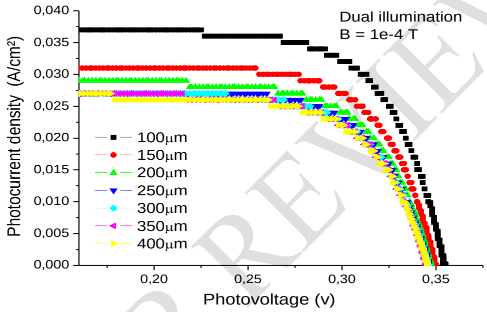

Figure 10: Photocurrent density as a function of photovoltage for various base thicknesses under dual illumination

At $B = 10^{-4}\ T$, figures 8, 9, and 10 show the $J_{ph} - V_{ph}$ curves for different illumination modes and base thicknesses.

- Front illumination: the influence of thickness is small because the junction is on the illuminated side; as long as the diffusion length exceeds the active base thickness and back-surface reflection lengthens the optical path, carrier collection remains efficient.
- Rear illumination: photogeneration occurs far from the junction; collection then becomes sensitive to the pair (H, L) and to the SRV, so increasing H lengthens the diffusion path, enhances recombination losses, and degrades both J_{ph} and V_{ph}.
- Dual illumination: bilateral generation improves both current and voltage; our data typically give $J_{sc} \approx 0.037\ A \cdot cm^{-2}$ and $V_{oc} \simeq 0.35$ V, consistent with the bifacial literature [14, 15].

Overall, $H \approx 100\ \mu m$ offers the best trade-off, consistent with an optimum thickness governed by surface quality: with low SRV (good passivation), thinning can raise V_{oc} while maintaining a high J_{sc} up to the point where optical losses appear; when SRV are higher, increasing H mainly promotes recombination and penalizes performance [4]. In all three modes, a nearly flat plateau is observed at low V_{ph} ($V_{ph} \approx J_{sc}$), followed by a rapid drop to zero at V_{oc}.

To interpret low-voltage trends (near short circuit) with precision, it is necessary to analyze how the shunt resistance depends on base thickness and, more broadly, on magnetic field, that is, $R_{sh}(H, B)$, via parametric extraction from the $\mathrm{J-V}$ curves alongside $\mathrm{J_0}$ and the ideality factor n. Specifically, the initial slope of the $\mathrm{J-V}$ trace (around $V \approx 0\mathrm{V}$) sets the apparent R_{sh}, which directly impacts $\mathrm{J_{sc}}$ and the fill factor; leakage paths associated with surface/bulk defects, grain boundaries, or micro-shunts reduce $\mathrm{J_{sc}}$ [2, 16, 17]. From a technology standpoint, good surface passivation (low SRV) increases $\mathrm{J_{sc}}$ and suppresses leakage, explaining why base thinning can remain beneficial as long as the diffusion length exceeds the active base thickness. Under magnetic bias, transport modifications (diffusivity D, Lorentz-force-perturbed trajectories) can manifest as a measurable change in the low-voltage slope and thus in the apparent $\mathrm{J_{sc}}$, consistent with the $\mathrm{I-V}$ evolutions reported for Si cells/modules under B [10, 12]. In this framework, a robust estimate of $R_{sh}(H, B)$, supplemented by defect-imaging methods (lock-in thermography, voltage-dependent electroluminescence), helps explain the limitation of $\mathrm{J_{sc}}$ and FF losses even when $\mathrm{V_{oc}}$ is only weakly affected [2, 16].

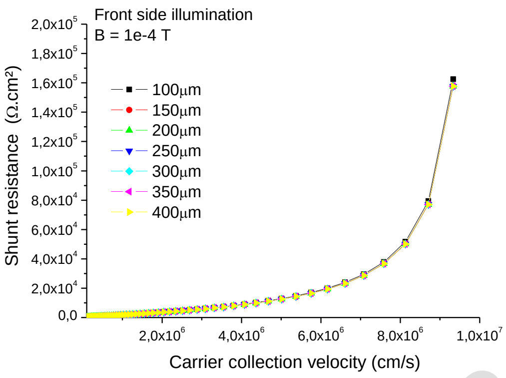

Figure 12: Shunt resistance as a function of carrier-collection velocity for various base thicknesses under front-side illumination, with $B = 10^{-4}\ T$

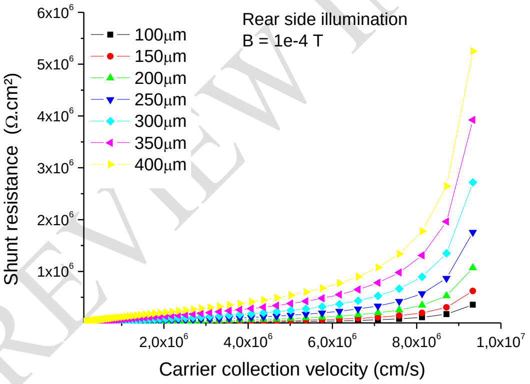

Figure 11: Shunt resistance as a function of carrier-collection velocity for various base thicknesses under rear-side illumination, with $B = 10^{-4}\ T$

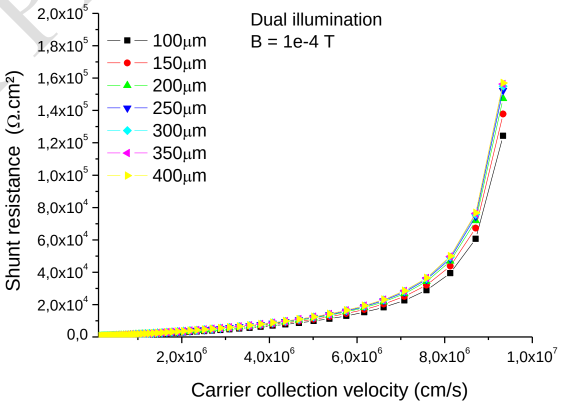

Figure 13: Shunt resistance as a function of carrier-collection velocity for various base thicknesses under dual illumination, with $B = 10^{-4}\ T$

At B = 10^{-4} T, figures 11, 12, and 13 show how the shunt resistance (R_{sh}) varies with the CCV for several base thicknesses and the three illumination modes. Overall, R_{sh} increases with CCV in all configurations: values reach $\sim 1{,}6.10^5 \Omega \cdot cm^2$under front illumination (Fig. 11) and dual illumination (Fig. 13), while rear illumination (Fig. 12) yields higher levels, on the order of $5.10^6 \Omega \cdot cm^2$. The plots can be interpreted in three CCV regimes:

i) 10^5 to 2.10^6 cm/s, where all three figures show a similar behavior with an apparent R_{sh}that is very low (near zero) regardless of mode and thickness;

ii) 2.10^6 to 8.10^6 cm/s, where Figures 11 and 13 display superposed curves and a monotonic rise of $R_{sh}$for all thicknesses, whereas under rear illumination (Fig. 12) R_{sh}remains nearly zero for $\mathrm{H} = 100 - 200$ μm; and

iii) beyond $8.10^6 cm/s$, the superposition persists for Figures 11 and 13, while under rear illumination the curves separate for H > 200 μm and maintain this gap.

Physically, the apparent R_{sh}inferred from the low-voltage slope of the $\mathrm{J}-\mathrm{V}$ curve depends on injection and illumination geometry: near-junction front or dual illumination raises injection, “seals” leakage paths, and increases R_{sh}; conversely, when photogeneration is far from the junction (rear) and the base becomes thicker, the diffusion distance and the SRV amplify micro-leakage (surface/bulk defects, grain boundaries), keeping R_{sh}low and then producing thickness-dependent dispersion at high CCV [2, 16, 17]. These observations are consistent with parametric extraction of R_{sh}(together with J_0, n, and R_s) from $\mathrm{J}-\mathrm{V}$ characteristics, and with imaging diagnostics (voltage-dependent electroluminescence, lock-in thermography) that reveal the local, distributed nature of leakage paths [2, 16]. In the bifacial context, bilateral generation further explains the higher R_{sh}values observed under dual illumination, in line with recent literature [14, 15].

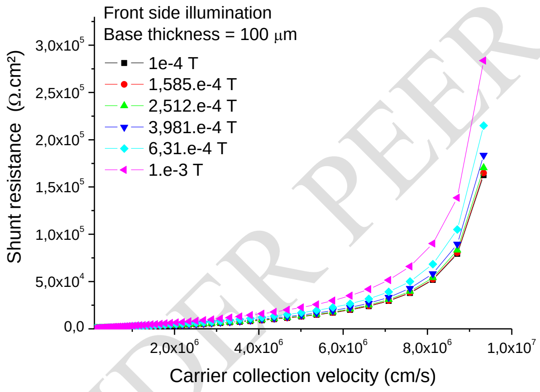

Figure 15: Shunt resistance as a function of carrier-collection velocity for different magnetic-field values B, under front-side illumination, at a base thickness of $e = 100\, \mu m$

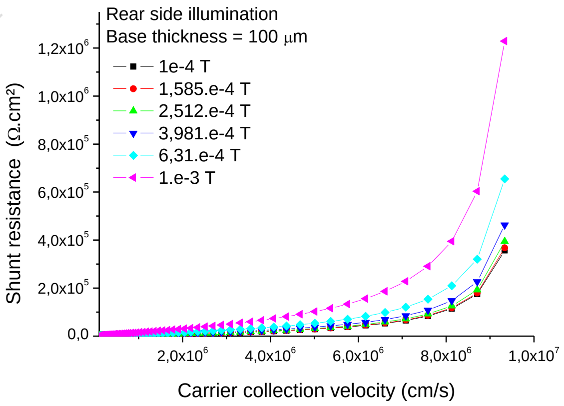

Figure 14: Shunt resistance as a function of carrier-collection velocity for different magnetic-field values B, under rear-side illumination, at a base thickness of $e = 100\, \mu m$

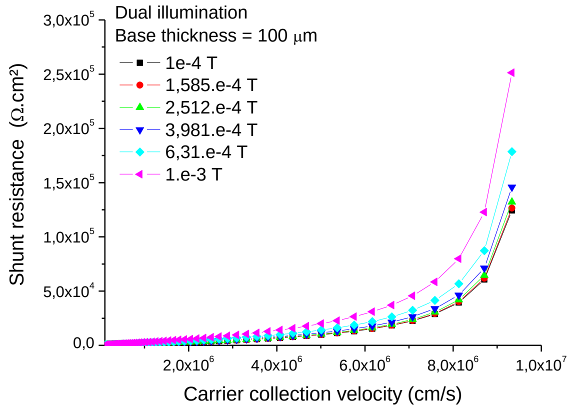

Figure 16: Shunt resistance as a function of carrier-collection velocity for different magnetic-field values B, under dual illumination, at a base thickness of $e = 100\,\mu m$

At $H = 100\ \mu m$, Figures 14, 15, and 16 show how the shunt resistance R_{sh} varies with the CCV for several base thicknesses and for the three illumination modes (front, rear, dual). In all modes, R_{sh} increases monotonically as CCV increases; it also rises with B. We further observe that the values under rear illumination are markedly higher ($\approx 4\times$) than those measured under front and dual illumination, while the magnetic-field effect is noticeably stronger under rear illumination. This ordering can be explained by the “apparent” nature of R_{sh} extracted at low voltage: when photogeneration occurs far from the junction (rear), the longer diffusion distance and the more influential SRV modulate leakage pathways (surface/bulk defects, grain boundaries), so the low-voltage slope of the $J-V$ curve, and hence R_{sh}, varies more strongly with CCV and B. Conversely, dual illumination raises injection on both sides, “seals” micro-leakage, and yields higher, less B-sensitive R_{sh} values, consistent with parametric extraction of R_{sh} (together with J_0, n, and R_s) and with electroluminescence/thermography diagnostics that reveal the local, distributed nature of leakage [2, 16]. These trends align with the literature on passivation (low SRV → high R_{sh}), the dependence on thickness/diffusion path, and the benefits of bifacial operation, as well as with the effects of magnetic field on transport and magnetoconductivity [10, 12, 14,15, 18].

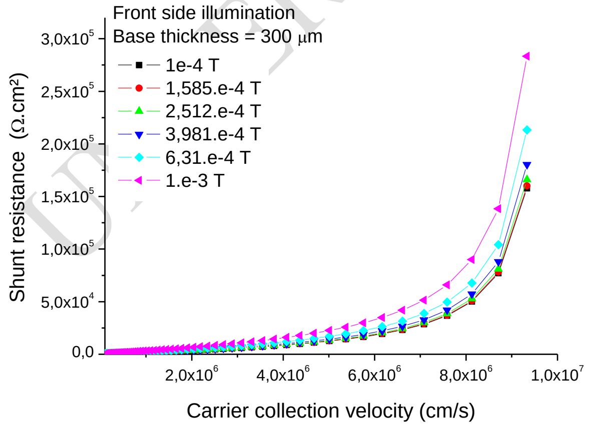

Figure 18: Shunt resistance as a function of carrier-collection velocity for different magnetic-field values B, under front-side illumination, at a base thickness of $e = 300\,\mu m$

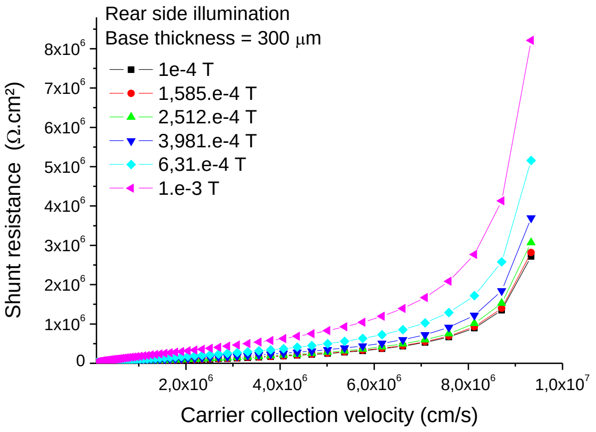

Figure 17: Shunt resistance as a function of carrier-collection velocity for different magnetic-field values B, under rear-side illumination, at a base thickness of $e = 300\,\mu m$

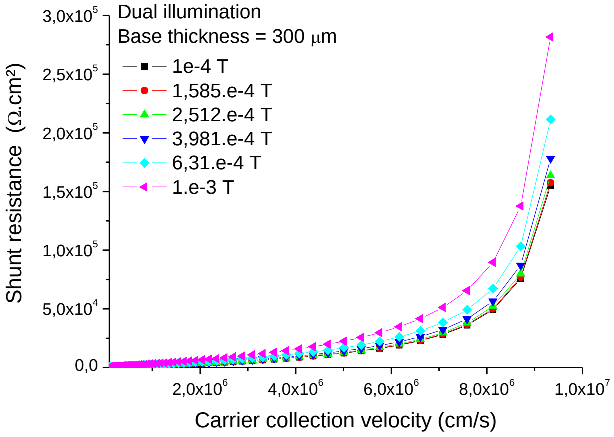

Figure 19: Shunt resistance as a function of carrier-collection velocity for different magnetic-field values B, under dual illumination, at a base thickness of $e = 300\,\mu m$

At $H = 300\ \mu m$, Figures 17, 18, and 19 show how the shunt resistance R_{sh} varies with magnetic field B for the three illumination modes (front, rear, dual). The profiles mirror those of Figures 14–16 (the $H = 100\ \mu m$ case): R_{sh} increases with B regardless of mode. Under front and dual illumination, the levels remain of the same order as at $H = 100\ \mu m$. By contrast, under rear illumination, the values extracted at $H = 300\ \mu m$ are about three times higher than those measured at $H = 100\ \mu m$, which suggests a partial closure of leakage paths and an "apparent extraction" effect linked to the low-voltage slope. Physically, the R_{sh} inferred near V≈0 reflects the density of micro-shunts and the SRV: effective passivation and/or more homogeneous injection tend to raise R_{sh}, whereas a longer diffusion distance and the presence of surface/bulk defects have the opposite effect [4, 17]. In addition, the magnetic field can modulate injection and local conductivity (magnetoconductivity), inducing measurable changes in the low-voltage slope and thus in the "apparent R_{sh}," with heightened sensitivity when photogeneration occurs far from the junction (rear illumination) [10, 12, 18]. These observations are consistent with parametric extractions $\{J_0,\ n,\ R_s,\ R_{sh}\}$ from $J - V$ curves, as well as with imaging diagnostics (voltage-dependent electroluminescence, lock-in thermography) that highlight the local and distributed nature of leakage paths [2, 16].

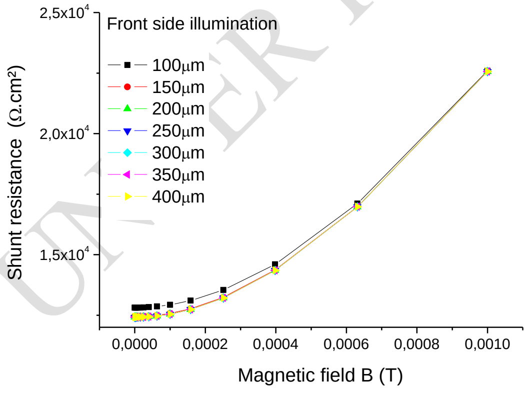

Variation of the Shunt resistance as a function of the magnetic field B for different values of the base thickness under front-side illumination.

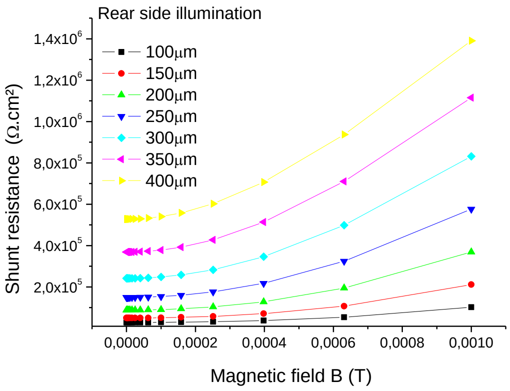

Variation of the Shunt resistance as a function of the magnetic field B for different values of the base thickness under rear-side illumination

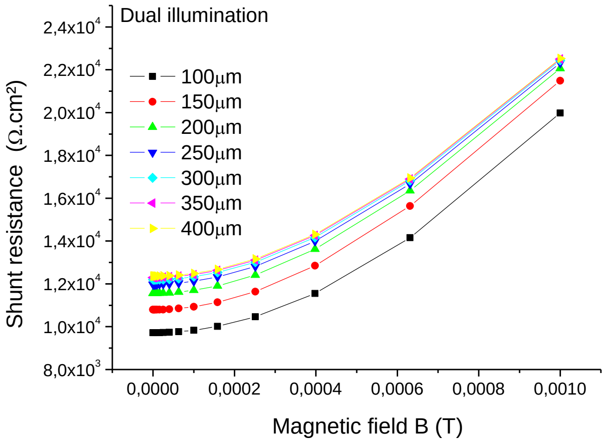

Figure 22:Variation of the Shunt resistance as a function of the magnetic field B for different values of the base thickness under dual illumination.

Under a variable magnetic field B (10^{-4} to 10^{-3}T), figures 20, 21, and 22 show a systematic increase in shunt resistance R_{sh} as B rises, for all illumination modes. The effect is clearly stronger under rear illumination: when the base thickness exceeds $\sim 250\ \mu m$, R_{sh} can increase by more than half a decade over the B range considered. Under rear and dual illumination, R_{sh} also increases with base thickness, whatever the value of B. By contrast, under front illumination, a very slight decrease in R_{sh} is observed as thickness increases. This ordering is explained by the “apparent” nature of R_{sh} derived from the low-voltage slope: when photogeneration is far from the junction (rear), the longer diffusion distance and more influential SRV make leakage paths (surface/bulk micro-shunts, grain boundaries) particularly sensitive to B; magnetoconductivity (Lorentz deflection, reduced mobility and thus reduced effective diffusivity) alters local injection and produces a steeper low-voltage slope, yielding a higher apparent R_{sh}, especially for large thicknesses [10, 12, 18]. In dual illumination, bilateral injection tends to “seal” micro-leakage and raises R_{sh} while mitigating the impact of B; in front illumination, the proximity of the junction maintains efficient collection, and increasing thickness can raise the likelihood of bulk defects, leading to the small decrease in R_{sh} that is observed. These findings are consistent with parametric extraction methods $\{J_0, n, R_s, R_{sh}\}$ from $J-V$ curves and with imaging diagnostics (voltage-dependent electroluminescence, lock-in thermography) that demonstrate the local and distributed nature of leakage paths [2, 16], as well as with the literature on passivation/thickness and bifacial operation [14, 15].

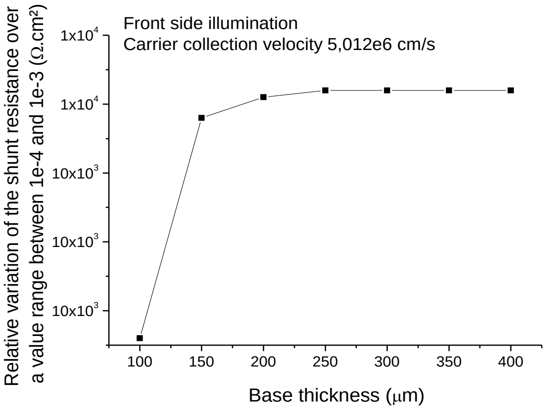

Figure 20: Absolute change in shunt resistance as a function of base thickness over the magnetic-field range $B = 10^{-4}\ to\ 10^{-3}\ T$, under front-side illumination

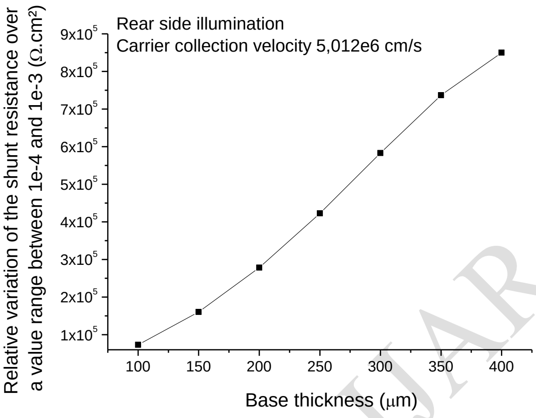

Figure 21: Absolute change in shunt resistance as a function of base thickness over the magnetic-field range $B = 10^{-4}\ to\ 10^{-3}$, under rear-side illumination

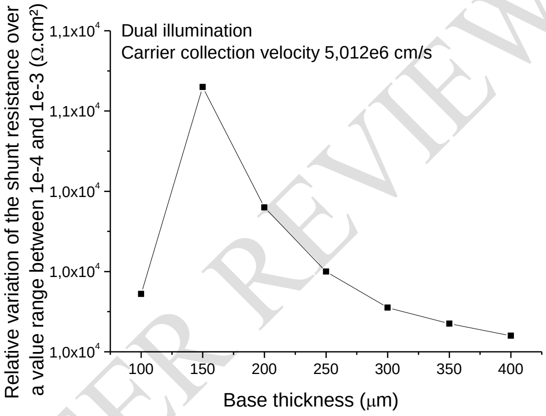

Figure 22: Absolute change in shunt resistance as a function of base thickness over the magnetic-field range$B = 10^{-4}\ to\ 10^{-3}\ T$, under dual illumination

At $CCV = 5.012 \times 1e6\ cm/s$, Figures 23–25 present the relative change in shunt resistance, denoted here as $\Delta_{rel}\ R_{sh}$, between $B = 10^{-4}$an$10^{-3}\ T$, as a function of base thickness and illumination mode.

i) Figures 23 and 25: two regions emerge. In region 1 ($100 - 150\ \mu m$), $\Delta_{rel}R_{sh}$ increases nearly linearly with thickness. In region 2 ($\geq 150\ \mu m$), the behaviors diverge: in Figure 23, $\Delta_{rel}R_{sh}$ remains high up to 400 µm, whereas in Figure 25 it gradually decreases toward lower values.

ii) Figure 24: $\Delta_{rel}R_{sh}$increases linearly with thickness over the entire interval.

Physically, a high R_{sh} is desirable because it limits leakage and supports both $J_{sc}$and the fill factor. The observed trends can be attributed to the "apparent" nature of R_{sh}extracted at low voltage: when photogeneration occurs near the junction (front illumination) or (dual illumination), the more uniform injection "seals" micro-shunts and stabilizes the initial $\mathrm{J - V}$ slope, yielding a plateau (Fig. 23) or an attenuation (Fig. 25) of $\Delta_{rel}\,R_{sh}$at large thickness. By contrast, when generation is far from the junction (rear illumination), the longer diffusion path and more influential SRV increase the sensitivity of the low-voltage slope to leakage paths (surface/bulk defects, grain boundaries), producing a sustained rise of $\Delta_{rel} R_{sh}$ with thickness (Fig. 24) [14, 15]. Finally, small thickness changes can have a disproportionate effect on R_{sh} when passivation is imperfect or when illumination alters the balance of resistive pathways; hence the value of a joint extraction $\{J_0,\ n,\ R_s,\ R_{sh}\}$ and imaging (voltage-dependent electroluminescence, lock-in thermography) to separate local leakage from extraction artifacts [2, 16, 17].

Conclusion

This study mapped how the shunt resistance, R_{sh}, evolves with base thickness and magnetic field across front, rear, and dual illumination modes, focusing on the low-voltage (near short-circuit) regime where the initial $J - V$ slope sensitively reflects leakage. Three robust trends emerged. First, R_{sh} increases with carrier-collection velocity and generally with magnetic flux density in the range $B = 1 \times 1e - 4$ to $1 \times 1e - 3\ T$, but the magnitude of the change depends strongly on illumination geometry: rear illumination, where photogeneration is far from the junction, exhibits the largest sensitivity, while dual illumination yields the highest and most stable R_{sh} owing to bilateral injection that "seals" micro-leakage pathways [14, 15]. Second, the thickness lever is decisive: thinning toward $\sim 100\ \mu m$ tends to raise R_{sh} (provided surface passivation is effective), whereas increasing thickness lengthens diffusion paths, elevates the influence of surface/bulk defects and grain boundaries, and lowers the apparent R_{sh} under rear illumination [4]. Third, the magnetic-field dependence is consistent with magneto-transport arguments, Lorentz-force perturbation of trajectories reduces mobility/diffusivity and modifies the low-voltage slope, so the extracted (apparent) R_{sh} can rise with B, especially when generation is remote from the junction [10, 12, 18].

Methodologically, our results underline the need for joint parameter extraction $\{J_0,\ n,\ R_s,\ R_{sh}\}$ over well-defined voltage windows, complemented by imaging diagnostics (voltage-dependent electroluminescence and lock-in thermography) to distinguish truly local leakage from extraction artefacts in distributed devices [2, 16]. Practically, the maps $R_{sh}(e, B)$ provide actionable guidance for thickness/passivation targets and for operating/measurement protocols:

i) prioritize high-quality passivation (low SRV) and moderate base thickness to stabilize R_{sh};
ii) leverage dual illumination in bifacial operation to mitigate leakage;
iii) account for magnetic-field effects, environmental or process-induced, during characterization near $V \approx 0$ so that apparent changes in R_{sh} are not misattributed to diode parameters.

Limitations of this work (idealized passivation in the model, simplified treatment of grain-boundary statistics, and fixed temperature) suggest several extensions: temperature-dependent magnetoconductivity, orientation/angle-of-incidence studies of B, and explicit 3D reconstructions of leakage networks in multicrystalline silicon. Together, these steps would refine the quantitative link between device architecture, magnetic environment, and the stability of R_{sh} in next-generation bifacial c-Si cells.

List Abbreviations:

3D: Three-dimensional
AM1.5: Standard solar spectrum (air mass 1.5)
B: Magnetic field (tesla, T)
BSF: Back Surface Field
c-Si: Crystalline silicon
CCV: Carrier-collection velocity ($cm \cdot s^{-1}$)

D: Diffusion coefficient ($cm^2 \cdot s^{-1}$)
D*: Effective diffusion coefficient under magnetic field
FF: Fill factor
G(z): Depth-dependent generation rate
H: Base thickness (µm)
J: Current density ($A \cdot cm^{-2}$)
J_{ph}: Photocurrent density
J_{sc}: Short-circuit current density
J_0: Diode saturation current density
L: Diffusion length (µm)
L*: Effective diffusion length under magnetic field
µ: Carrier mobility ($cm^2 \cdot V^{-1} \cdot s^{-1}$)
n: Diode ideality factor
PV: Photovoltaic
q: Elementary charge of the electron (C)
R_s: Series resistance ($\Omega \cdot cm^2$)
R_{sh}: Shunt resistance ($\Omega \cdot cm^2$)
SCR: Space-charge region
S_b: Effective rear-surface recombination velocity
S_f: Effective front-surface recombination velocity
S_{f0}: Intrinsic junction term
S_{fj}: Load-induced front-surface recombination component
S_g: Grain-boundary recombination velocity
SRV: Surface recombination velocity ($cm \cdot s^{-1}$)
τ: Minority-carrier lifetime (s)
V: Terminal voltage (V)
V_{oc}: Open-circuit voltage (V)
V_{ph}: Photovoltage (V)

Références

[1] S. M. Sze and K. K. Ng, Physics of Semiconductor Devices, 3rd ed. Hoboken, NJ, USA: Wiley, 2006.

[2] Hinken, D. et al., "Series resistance imaging of solar cells by voltage-dependent electroluminescence," Appl. Phys. Lett. 91 (2007) 182104. https://doi.org/10.1063/1.2804562.

[3] M. TOURE and al, "3D Mathcad Simulation of Photogenerated current density in C-Si Solar Cells Under Multispectral Illumination: Combined Effect of Transverse Magnetic Field and Base Thickness", International Journal of Materials Science and Applications 2025, Vol. 14, No. 4, pp. 172-184 https://doi.org/10.11648/j.ijmsa.20251404.16

[4] C.-H. Lin, "The Effect of Thickness and Surface Recombination Velocities on the Performance of Silicon Solar Cell," Solids 6 (2025) 33. https: //doi.org/10.3390/solids6030033.

[5] Liu, S., Zhang, M., & Wang, X. (2019). Enhanced bifacial solar cell performance through 3D modeling. Renewable Energy, 135, 1427–1434. https://doi.org/10.1016/j.renene.2018.12.062

[6] A. Dieng and al., "Determination of the optimal base thickness of an n+–pp+ silicon solar cell under magnetic field," in Proc. 24th Eur. Photovoltaic Solar Energy Conf., 2009.

[7] M Zoungrana and all, "The effect of magnetic field on the efficiency of a silicon solar cell under an intense light concentration" Advances in Science and Technology Research Journal Volume 11, Issue 2, June 2017, pages 133–138 https://doi.org/10.12913/22998624/69699

[8] D. K. Schroder, Semiconductor Material and Device Characterization, 3rd ed. Hoboken, NJ, USA: Wiley, 2006.

[9] C. Thiaw and al., “Determination of the optimal base thickness of an n+–pp+ silicon solar cell under magnetic field,” J. Electromagn. Anal. Appl., vol. 12, no. 7, pp. 139–154, 2020 https://doi.org/10.4236/jemaa.2020.127009.

[10] Fathabadi, H. (2020). Magnetic field effect on silicon based solar cells. Materials Chemistry and Physics, 244, 122684. https://doi.org/10.1016/j.matchemphys.2020.122684. ScienceDirect

[11] Combari, D. U. and al. (2018). Performance Investigation of a Silicon Photovoltaic Module under the Influence of a Magnetic Field. Advances in Condensed Matter Physics, 2018, Article ID 6096901. https://doi.org/10.1155/2018/6096901. Wiley Online Library

[12] Ndeto, M. P., Wekesa, D. W., Kinyua, R., & Njoka, F. (2020). Investigation into the effects of the earth’s magnetic field on the conversion efficiency of solar cells. Renewable Energy, 159, 184–194. https://doi.org/10.1016/j.renene.2020.05.143. ScienceDirect

[13] Faye, D. et al., “Lamella Silicon Solar Cell under Both Temperature and Magnetic Field: Width Optimum Determination,” J. Electromagn. Anal. Appl. **12** (2020) 43–55. **https://doi.org/**10.4236/jemaa.2020.124005.

[14] T. S. Liang et al., “A review of crystalline silicon bifacial photovoltaic performance characterisation and simulation,” Energy Environ. Sci. 12 (2019) 116–148.https://doi.org/10.1039/C8EE02184H.

[15] R. Guerrero-Lemus et al., “Bifacial solar photovoltaics – A technology review,” Renew. Sustain. Energy Rev. 60 (2016) 1533–1549. https://doi.org/10.1016/j.rser.2016.03.041.

[16] Breitenstein, O. et al., “Series resistance imaging in solar cells by lock-in thermography,” Prog. Photovolt. 13 (2005) 645–660. https://doi.org/10.1002/pip.623.

[17] Tada, K. et al., “What do apparent series and shunt resistances in solar cells really mean?,” phys. status solidi (a) 215 (2018) 1800448. https://doi.org/10.1002/pssa.201800448

[18] Sourabié, I.; Zerbo, I.; Zoungrana, M.; Combari, D. U.; Bathiebo, D. J. (2017). Effect of Incidence Angle of Magnetic Field on the Performance of a Polycrystalline Silicon Solar Cell under Multispectral Illumination. Smart Grid and Renewable Energy, 8, 325–335.https://doi.org/10.4236/sgre.2017.810021.